

# Effect of anodic oxidation on the corrosion behavior of Ti-based materials in simulated physiological solution

Ingrid Milošev · Diana Blejan · Simona Varvara ·  
Liana Maria Muresan

Received: 17 January 2013 / Accepted: 29 April 2013 / Published online: 16 May 2013  
© Springer Science+Business Media Dordrecht 2013

**Abstract** Anodic oxidation in acetic acid was investigated as a means of improving the corrosion resistance, in simulated physiologic solution, of titanium and two titanium-based alloys, Ti–6Al–7Nb and Nitinol. The composition and the thickness of the surface layers formed by anodization were analyzed using X-ray photoelectron spectroscopy. The electrochemical characteristics were investigated by linear polarization, cyclic polarization, and electrochemical impedance spectroscopy at the open circuit potential. Anodization of all these three metals resulted in the formation of TiO<sub>2</sub> as the main oxide. These layers improved the corrosion behavior in simulated physiological solution, as evidenced by significant increase in polarization resistance and decrease in corrosion current density. Electrochemical impedance results were interpreted based on the two-layer structure of the passive film. Anodization has thus been shown to provide a simple and effective means of improving the corrosion behavior of titanium-based alloys in simulated physiological solution.

**Keywords** Ti-based alloys · Simulated physiological solution · Anodic oxidation · X-ray photoelectron spectroscopy · Electrochemical impedance spectroscopy

## 1 Introduction

Over the past 40 years, titanium and its alloys have been used widely as dental and implant materials because of their very good biocompatibility, corrosion resistance, and mechanical properties. In order to improve the integration of orthopedic implants in the host bone tissue and reduce the corrosion resistance of the implants, bioactive and TiO<sub>2</sub> films, respectively, have been applied as coatings on the metallic substrates [1–3]. Due to its biocidal activity, the deposition of a TiO<sub>2</sub> layer on the implant surface may serve to reduce the infection that arises from the adherence and colonization of the bacteria [4].

TiO<sub>2</sub> films have been prepared using methods such as sputtering [5], chemical vapor deposition [5, 6], sol–gel [7], and electrodeposition [8]. Ag–TiO<sub>2</sub> composite nanofilms have been recognized as showing stronger bactericidal activity than TiO<sub>2</sub> nanofilms, both in the dark and the under UV illumination [9]. Ceramic films can be produced by techniques which include the relatively simple and cost effective electrophoretic deposition method [10]. Particles deposited on the electrode form a relatively dense and homogeneous film. Sol–gel methods have resulted in TiO<sub>2</sub> films with a variety of crystalline structures and porosities [11].

Titanium oxide films can also be produced by anodization, a simple and low-temperature process resulting in the formation of smooth oxide layers free of cracks and pores [12–15]. Anodization can be performed in a number of electrolytes with growth rates of the order of 2 nm V<sup>−1</sup>. The thickness can reach several hundred nanometers [12]. The oxide film that consists of TiO<sub>2</sub> can possess a certain degree of nonstoichiometry [12]. Sul et al. [13] studied the galvanostatic oxidation of titanium in various electrolytes as a function of various experimental parameters. Different

I. Milošev (✉)  
Department of Physical and Organic Chemistry,  
Jožef Stefan Institute, Jamova c. 39, 1000 Ljubljana, Slovenia  
e-mail: ingrid.milosev@ijs.si

D. Blejan · L. M. Muresan  
Department of Chemical Engineering, Babes-Bolyai University,  
400028 Cluj-Napoca, Romania

S. Varvara  
Department of Topography, 1 Decembrie 1918 University,  
510009 Alba-Iulia, Romania

oxide thicknesses were reflected in different colors and were dependent on the forming voltage. The dependence of the oxide thickness on anodic voltage was higher in acid than in the alkaline electrolytes. Breakdown voltages are strongly dependent on the nature of the electrolyte and are lower in acid (100 V) than in alkaline solutions (up to 200 V) [12]. In solutions of KOH, the concentration of the latter strongly affects the breakdown voltage, as well as the potential at which the oxide film is transformed from amorphous to crystalline form, i.e., anatase, brookite, corundum, or rutile [16]. Brookite and corundum are the intermediate forms of anodic oxide films and the final form is composed primarily of an anatase type of  $\text{TiO}_2$  [16]. Arsov et al. [17] studied both the potentiostatic and the galvanostatic electrochemical oxidations in  $\text{H}_2\text{SO}_4$ , KOH, and  $\text{HNO}_3$  solutions by in situ Raman spectroscopy. The transformation of amorphous Ti-oxide to anatase, brookite, and rutile forms was dependent on the nature and concentration of the electrolyte, the applied voltage and current; and the anodization time. Increasing the voltage leads to a progressive transformation of anatase to rutile forms—unless extremely high voltages are applied, anatase formation always precedes the formation of rutile. This crystallographic transformation is closely related to the breakdown of the oxide film.

The oxidation of titanium alloys has received much less attention than that of the titanium. Anodic films have been grown on Ti and on Ti–6Al–4V alloy in chromic acid (CA) and in CA-containing hydrofluoric acid (CA/HF) [18]. The compact films grown on Ti–6Al–4V alloy in CA were amorphous, and the porous films grown in CA/HF solution were partially crystalline. The composition of the films on titanium substrate corresponds to that of  $\text{TiO}_2$ , and, on the Ti–6Al–4V substrate, to  $\text{TiO}_2 + \text{Al}_2\text{O}_3$  (with a Ti/Al ratio of 5).

Besides Ti–6Al–4V alloy, other titanium-based alloys—Ti–6Al–7Nb and Nitinol alloys—are used in biomedical applications. In the former, the potentially cytotoxic vanadium [19, 20] has been replaced by inert niobium, resulting in an alloy whose mechanical properties are better than those of the Ti–6Al–4V alloy [21]. Nitinol (NiTi) is the commercial name for an alloy containing nearly equi-atomic contents of nickel and titanium [22]. Whereas Ti–6Al–Nb alloy is used mainly for the manufacture of femoral components of hip prostheses; Nitinol has been explored mainly in the orthodontic treatment, in cardiovascular surgery for stents and guide wires, and in orthopedic surgery for various staples [23]. Its applications are based on its properties of shape memory and superelasticity [23]. The corrosion resistance of Nitinol is worse than that of other the titanium-based alloys [24]. Furthermore, nickel is a known allergen, so it is desirable to keep its concentration as low as possible to avoid its dissolution in the

periprosthetic tissue when implanted in the human body. Therefore, the improved corrosion resistance and the increased biocompatibility of Nitinol under physiological conditions are required, since other titanium-based alloys used in biomedical applications do not possess its unique properties and thus cannot replace this material.

Anodization in acetic acid has been reported to be an effective means of producing an oxide layer on Nitinol, improving its corrosion and biocompatibility properties [25–27]. Shi et al. [25] anodized Nitinol galvanostatically in 1 M acetic acid, the optimal conditions being  $20 \text{ mA cm}^{-2}$  for 1 h which produced  $\text{TiO}_2$  layers 20–25-nm thick. The ratio Ti/Ni in this anodized layer was 33:1, much higher than in the bulk material where the ratio is 1:1. Nickel was present in both the metal and the oxidized states, i.e., as  $\text{Ni}_2\text{O}_3$  [26]. Titanium was oxidized to  $\text{TiO}_2$ , but sub-oxides  $\text{TiO}$  and  $\text{Ti}_2\text{O}_3$  were observed within the layer during the sputtering process [26]. Chu et al. [27] fabricated a  $\text{TiO}_2$  layer galvanostatically in 0.02 M  $\text{Na}_2\text{SO}_4$  solution, pH 3.0, at 0.3 mA for 1 h. The thickness of this layer was about 100 nm. It contained no detectable nickel at the outermost surface of the layer. Potentiostatic oxidation of Nitinol in acetic acid also produced a  $\text{TiO}_2$  layer <10-nm thick [28]. The incorporation of nickel into a  $\text{TiO}_2$  layer was dependent on the electrode potential. At potentials more negative than 0.75 V versus SCE, it was present as metal while, at higher potentials, it was oxidized to NiO [28]. The Ti/Ni ratio was high and, depending on the electrode potential, ranged from 8.1 to 11.5 [28]. Besides anodization, other treatments for improving the corrosion resistance were investigated in our previous reports, like boiling in water and thermal oxidation [29], and self-assembly of organic molecules [30]. Both the procedures produced  $\text{TiO}_2$  layers greatly depleted in nickel.

It has been suggested that oxide layers formed by anodization differ according to the substrate, e.g., oxidation in CA produced a  $\text{TiO}_2$  layer on titanium substrate, but layers consisting of  $\text{TiO}_2$  and  $\text{Al}_2\text{O}_3$  oxides on a Ti–6Al–4V substrate [18]. Further, the oxide thickness increased with voltage at a rate of  $7 \text{ nm V}^{-1}$  on Ti, and  $5 \text{ nm V}^{-1}$  on the Ti–6Al–4V alloy. Although anodization in acetic acid was proved to be an effective treatment on Nitinol, it has not been studied systematically for other titanium-based materials. Sul et al. [13] anodized Ti galvanostatically in 1 M acetic acid at potentials from 40 to 100 V and obtained thicknesses between 71 and 234 nm. The impact of the oxide film formed on Ti and its Ti alloys on corrosion resistance in simulated physiological solution (SPS) has not been investigated. The aim of the present study was therefore to study and compare the effects of potentiostatic anodization in acetic acid on the corrosion behavior in SPS, using three titanium-based materials—titanium metal, Ti–6Al–7Nb and Nitinol alloys. Besides the electrochemical methods [linear

and cyclic polarization (CP) measurements and electrochemical impedance spectroscopy (EIS)] for the study of corrosion behavior, anodized layers were investigated in terms of chemical composition and layer thickness. For that purpose, X-ray photoelectron spectroscopy (XPS) combined with the depth profiling was used.

## 2 Materials and Methods

### 2.1 Materials and Sample Preparation

Three titanium-based materials were studied. Titanium metal (purity 99.6 %, annealed) was supplied by Goodfellow (Cambridge, Ltd., UK). Samples of Ti–6Al–7Nb alloy were cut from the femoral component of a total hip replacement manufactured by company Sulzer (Winthertur, Switzerland). Nitinol (NiTi) was the superelastic alloy S, supplied by Memry GmbH, Weil am Rhein, Germany. It was annealed and oxide free with a nominal composition of 50 at.% Ni and 50 at.% Ti. Titanium and NiTi were purchased in the form of 2-mm thick foil. Samples were cut in the form of discs of 15-mm diameter.

Samples were ground mechanically under water with, successively, 320, 500, 800, 1000, 1200, 2400 and 4000 grit SiC papers. Each sample was ground in one direction until all imperfections were removed and the surface was covered with a uniform pattern of scratches. They were then cleaned with ethanol in an ultrasonic bath for 2 min, double-rinsed with Milli-Q water, and finally dried in a stream of nitrogen.

### 2.2 Electrochemical measurements

Electrochemical measurements were performed in a conventional three-electrode cell (volume 300 mL) at a temperature of  $37 \pm 1$  °C. The working electrode was embedded in a Teflon holder, with an area of  $0.785 \text{ cm}^2$  exposed to the solution. Graphite was the counter electrode. Potentials were measured against a saturated calomel electrode (SCE) connected to the cell via a Luggin probe. Measurements were carried out with an Autolab PGSTAT 12 potentiostat/galvanostat (Metrohm Autolab, Utrecht, The Netherlands) controlled by Nova 1.7.

Prior to the measurement, samples were allowed to stabilize under open circuit potential,  $E_{oc}$ . During this time, the value of  $E_{oc}$  was measured as a function of time. The stabilization process was continued until the potential reached the stable, quasi-steady state value denoted as the corrosion potential,  $E_{corr}$ . This process usually took up to 2 h. Linear polarization was measured in the potential range  $\pm 10$  mV versus  $E_{corr}$ , using a  $0.1 \text{ mV s}^{-1}$  potential scan rate. Values of polarization resistance,  $R_p$ , were estimated from the slope of fitted current

density versus potential, using Nova software. Potentiodynamic polarization curves were measured using a  $1 \text{ mV s}^{-1}$  scan rate, starting at 250 mV negative to  $E_{corr}$  and then increased in the anodic direction. For each sample, measurements were performed in at least triplicate and the average measurement was chosen. For this measurement, curves and deduced corrosion parameters are presented in the Sec 3.

CP is based on forcing the material from its steady state by sweeping the potential in the anodic direction until some pre-determined switching potential ( $E_{sw}$ ) is reached. This technique involves the use of two important potentials—the breakdown or pit nucleation potential and the repassivation potential—to predict the susceptibility to localized corrosion breakdown [31].

For EIS measurements, a PARSTAT 2273 (Princeton Applied Research, USA) potentiostat was used. The frequency ranged from 10 kHz to 10 mHz at an ac voltage of  $\pm 5$  mV. Impedances were measured at the  $E_{oc}$  for untreated sample and sample oxidized in acetic acid after 0, 1, 2, 4, 6, 8, 10, 15, 24, 48, 72, 96, 120 and 140 h of immersion in the electrolyte. The impedance data were interpreted on the basis of different equivalent electrical circuits, using the ZSimpWin V3.21 software for fitting the experimental results.

Electrochemical measurements were performed at 37 °C in Hanks balanced salt solution—SPS— $8 \text{ g L}^{-1}$  NaCl,  $0.4 \text{ g L}^{-1}$  KCl,  $0.25 \text{ g L}^{-1}$   $\text{NaH}_2\text{PO}_4 \cdot 2\text{H}_2\text{O}$ ,  $0.35 \text{ g L}^{-1}$   $\text{NaHCO}_3$ ,  $0.06 \text{ g L}^{-1}$   $\text{Na}_2\text{HPO}_4 \cdot 2\text{H}_2\text{O}$ ,  $0.19 \text{ g L}^{-1}$   $\text{CaCl}_2 \cdot 2\text{H}_2\text{O}$ ,  $0.4 \text{ g L}^{-1}$   $\text{MgCl}_2 \cdot 6\text{H}_2\text{O}$ ,  $0.06 \text{ g L}^{-1}$   $\text{MgSO}_4 \cdot 7\text{H}_2\text{O}$ , and  $1 \text{ g L}^{-1}$  glucose. The pH was adjusted to 7.4 by adding HCl or NaOH (1 M) solution. All chemicals were of *p.a.* purity, and used as supplied by Applichem GmbH, Germany, Fluka, Germany, Sigma-Aldrich, Germany or Sigma Life Science, USA. Solutions were prepared in Milli-Q Direct water with a resistivity of  $18.2 \text{ M}\Omega \text{ cm}$  at 25 °C (Millipore, Billerica, MA).

Anodic oxidation of samples was carried out at room temperature in 1 M acetic acid, pH 2.3 for 2 h at 0.7 V for Ti, Ti–6Al–7Nb, and NiTi, and at 3.0 V for Ti and Ti–6Al–7Nb alloy. Acetic acid was supplied by J.T. Baker, The Netherlands.

### 2.3 X-ray photoelectron spectra

XPS were obtained using a TFA Physical Electronics Inc. spectrometer using non and monochromatized Al  $K\alpha$  radiation (1,486.6 eV) and a hemispherical analyzer. The monochromatized radiation used for high-resolution spectra yields a resolution of 0.6 eV, as measured on an Ag  $3d_{5/2}$  peak. These spectra were used to differentiate between various species, whereas spectra obtained using the nonmonochromatized variation were used for quantifying the chemical composition. The take-off angle used, defined as the angle of emission relative to the surface, was 45°. The energy

resolution was 0.5 eV. Survey scan spectra were recorded at pass energy of 187.85 eV and individual high-resolution spectra at pass energy of 23.5 eV with an energy step of 0.1 eV. After taking the surface spectra, depth profiles of the oxidized layers were determined. An  $\text{Ar}^+$  ion beam with an energy level of 3 keV and with a raster of  $4 \times 4$  mm (sputter rate  $4.0 \text{ nm min}^{-1}$  determined on the  $\text{SiO}_2$  standard), or of  $2 \times 2$  mm (sputter rate  $2.0 \text{ nm min}^{-1}$  determined on the  $\text{SiO}_2$  standard), was used for sputtering [32].

The XPS spectra were background subtracted, using the nonlinear, iterative Shirley method [33]. The fitting procedure allowed the signals to be evaluated by determining the peak position, height, width, and Gaussian/Lorentzian ratio [34]. Details are described in our previous publications [28, 29, 35–37].

The  $2p_{3/2}$  peak for Ti metal state is centered at 454.2 eV, and that for Ti in oxidized state at 459.2 eV. The  $2p_{3/2}$  peaks for titanium sub-oxides were located at 456.6 eV for  $\text{TiO}$ , and at 457.6 eV for  $\text{Ti}_2\text{O}_3$  [36, 37]. Ni metal shows a main  $2p_{3/2}$  peak at 851.8 eV with a satellite  $\sim 6.5$  eV at 858.3 eV. Nickel oxide ( $\text{NiO}$ ) shows a complex structure including the three peaks in the  $2p_{3/2}$  region (854.7, 856.5, and 861.7 eV) due to multiplet splitting and a monopole charge transfer process [37]. The center of the Al  $2p_{3/2}$  peak in aluminum metal is located at 71.5 eV, and, in  $\text{Al}_2\text{O}_3$ , at 74.8 eV [36]. The center of the Nb  $3d_{5/2}$  peak of niobium metal is located at 203.5 eV. Niobium can form oxides in three oxidation states,  $\text{NbO}$ ,  $\text{NbO}_2$ , and  $\text{Nb}_2\text{O}_5$ . The binding energy increases with the increasing degree of oxidation, i.e., from 204.5 eV for  $\text{NbO}$  and  $\text{NbO}_2$ , to 207.5–207.8 eV for  $\text{Nb}_2\text{O}_5$  [36]. The position of the center of the O  $1s$  peak depends on the hydration of the layer and ranges from 530.1 eV (oxide component,  $\text{O}^{2-}$ ) and 531.2 eV (hydroxide component,  $\text{OH}^-$ ) to 532.2 eV (water-containing species,  $\text{H}_2\text{O}$ ).

### 3 Results and discussion

#### 3.1 Anodization of Ti, Ti–6Al–7Nb, and NiTi in acetic acid

##### 3.1.1 Polarization curves and potentiostatic transients

Polarization curves were first measured, following stabilization at the open circuit potential, for Ti, Ti–6Al–7Nb, and NiTi in acetic acid, pH 2.3, to determine the conditions to be used for potentiostatic oxidation (Fig. 1a). The values of  $E_{\text{corr}}$  determined from the Tafel plots range from  $-0.25$  V for Ti to  $-0.098$  V for NiTi. The values of corrosion current density,  $j_{\text{corr}}$ , are  $32 \mu\text{A cm}^{-2}$  for Ti  $< 75 \mu\text{A cm}^{-2}$  for Ti–6Al–7Nb  $< 115 \mu\text{A cm}^{-2}$  for NiTi. Following the Tafel region, the current densities plateau out, indicating the passivity of all the three materials. At approximately 1.0 V, the current density

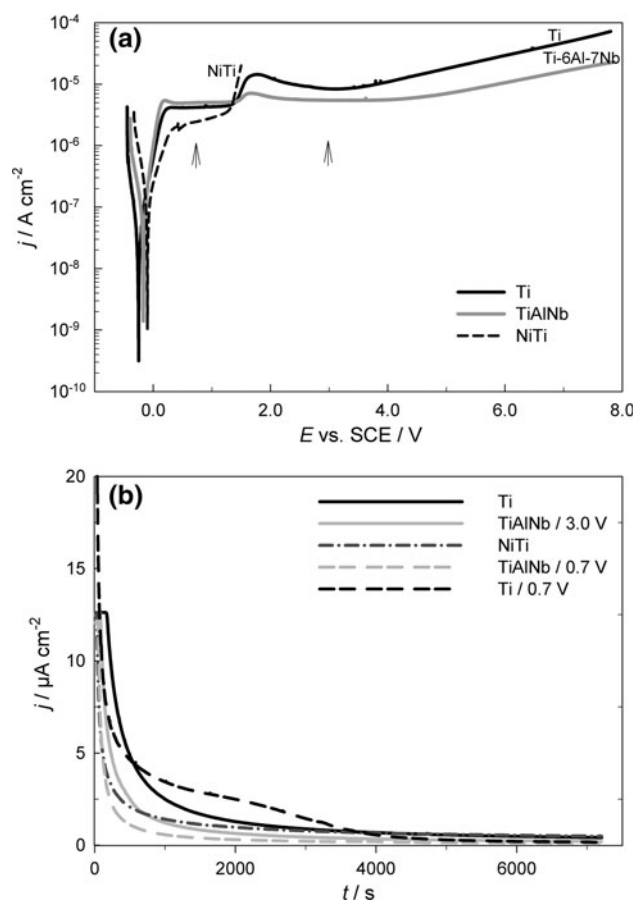


**Fig. 1** **a** Potentiodynamic polarization curves for Ti, Ti–6Al–7Nb, and NiTi recorded in 1 M acetic acid 1 M, pH 2.3, using a scan rate  $1 \text{ mV s}^{-1}$ . The oxidation potentials (0.7 and 3.0 V) are denoted by arrows. **b** Current versus time curves measured during potentiostatic oxidation at 0.7 and 3.0 V for 2 h in 1 M acetic acid

starts to increase. For NiTi, this increase is related to the breakdown of the passive range and the initiation of localized corrosion. In contrast, for Ti and Ti–6Al–7Nb alloy, the increase in the current density is followed by formation of a second current density plateau that extends from 2.5 V to high anodic potential of 8 V. In this potential range, only a slight increase in the current density is observed and the electrodes are considered to be in the passive state. Based on the polarization curves (Fig. 1a), the potentials within the well-developed passive state that are suitable for formation of the oxide layer on a particular material were selected: for Ti and Ti–6Al–7Nb alloy, two potentials were selected: 0.7 V in the first current density plateau, and 3 V in the well-developed second current density plateau. For NiTi, whose corrosion resistance is much lower than that of the other two materials, the potential of 0.7 V was selected. This potential is, approximately, in the middle of its passive region, and coincides with the first potential selected for the other two materials. The variations of the current density with time, recorded during potentiostatic oxidation (anodization) at selected

**Table 1** Chemical compositions deduced from XPS survey spectra measured at the surface of layers formed by potentiostatic oxidation of Ti, Ti–6Al–7Nb, and NiTi in 1 M acetic acid (1 M, pH 2.3) for 2 h

Element	Chemical composition (at.%)				
	$E_{\text{ox}} = 0.7 \text{ V}$			$E_{\text{ox}} = 3.0 \text{ V}$	
	Ti	Ti–6Al–7Nb	NiTi	Ti	Ti–6Al–7Nb
C 1s	44.7	20.6	38.0	29.5	34.7
O 1s	42.7	57.2	46.6	55.2	48.8
Ti 2p	12.6	16.8	13.3	15.3	13.2
Al 2p	–	3.9	–	–	1.8
Nb 3d	–	1.5	–	–	1.5
Ni 2p	–	–	2.1	–	–

Oxidation potentials,  $E_{\text{ox}}$ , were 0.7 and 3.0 V

potentials, are presented in Fig. 1b. Current density decreases continuously with time until it reaches a steady state (approximately after 1 h), and then remains at this low value to the end of the anodization period at 2 h. This behavior is related to the growth of a passive oxide layer at the surface. Variation of the decrease of current density with time indicates that the passive layers are formed at different rates on different substrates.

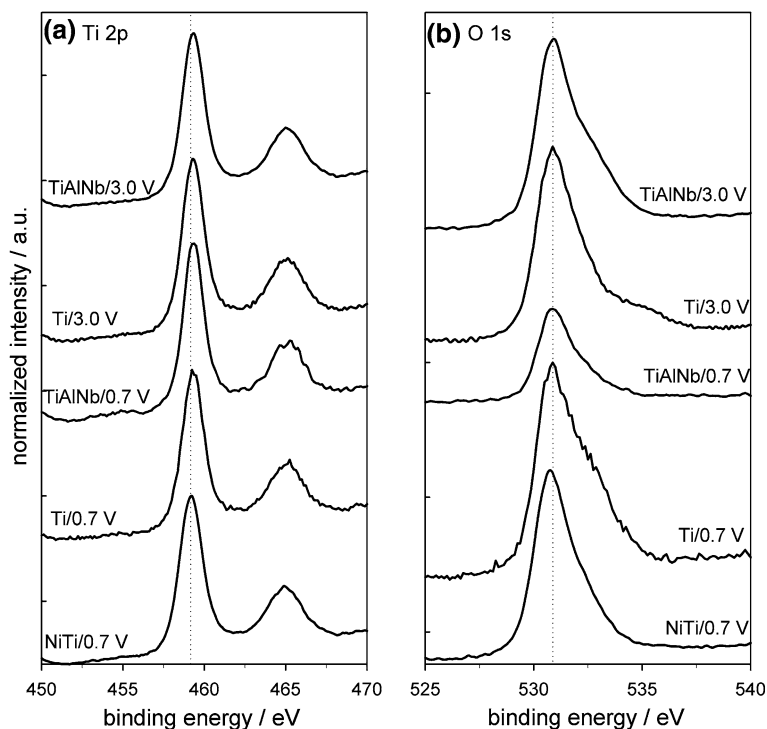
### 3.1.2 Composition of the oxide layer

The chemical composition of the surface was deduced from the XPS survey spectra (Table 1). The surface contains

abundant carbon due to air contamination during the transfer of the sample from the cell to the XPS chamber. The layer is comprised mainly of titanium and oxygen, confirming that titanium oxide is the major component of the layer formed by anodization of Ti, Ti–6Al–7Nb, and NiTi in acetic acid. The oxide layer formed on the alloys also contains minor elements. Besides Ti and O, the layer formed on Ti–6Al–7Nb contains minor levels of aluminum and niobium (totals of 5.4 and 3.3 at.% after oxidation at 0.7 and 3.0 V). The layer formed on NiTi contains 2.1 at.% Ni (the ratio of Ti/Ni is 6:3).

High-resolution XPS spectra revealed the chemical state of the elements in the layer. Normalized XPS spectra for Ti 2p and O 1s were recorded at the surfaces of Ti, Ti–6Al–7Nb, and NiTi oxidized at 0.7 and 3.0 V (Fig. 2). The center of the Ti 2p<sub>3/2</sub> peak is located at 459.2 eV for all the samples, confirming the presence of titanium(IV) oxide, TiO<sub>2</sub> (Fig. 2a). An example of spectrum deconvolution, using component peaks of Ti metal, Ti<sub>2</sub>O<sub>3</sub>, and TiO<sub>2</sub>, is presented in Fig. 3a and the intensities of the peaks obtained in Table 2. The surface layer is composed mainly of TiO<sub>2</sub> (>80 %) and only approximately 10 % of sub-oxide Ti<sub>2</sub>O<sub>3</sub>, independently of substrate and oxidation potential. Sub-oxide TiO is not taken into account since its intensity amounted to <1 % of the total intensity.

The center of the O 1s spectrum is located at 530.7 eV (Fig. 2b). The intensities of component peaks O<sup>2–</sup>, OH<sup>–</sup>, and H<sub>2</sub>O are presented in Table 2 for all the samples studied. Depending on the sample, the oxide component

**Fig. 2** Normalized XPS **a** Ti 2p and **b** O 1s spectra measured at the surface of Ti, Ti–6Al–7Nb, and NiTi oxidized at 0.7 and 3.0 V for 2 h in 1 M acetic acid



$\text{O}^{2-}$  comprised between 27.9 and 43.1 % of the intensity of the oxygen peak, the rest of intensity being due to hydroxide and water containing oxygen species. The surface layers formed are thus strongly hydrated, as expected for air-exposed samples. An example of spectral deconvolution using component peaks of  $\text{O}^{2-}$ ,  $\text{OH}^-$ , and  $\text{H}_2\text{O}$  is presented in Fig. 3b.

The surface layer formed on Ti–6Al–7Nb alloy contains, besides titanium and oxygen, the minor elements aluminum and niobium (Table 1). Deconvoluted Nb 3*d* and Al 2*p* spectra recorded at the layer formed at 3.0 V are presented in Fig. 4a, b. The spectra recorded after oxidation at 0.7 V are almost identical to those recorded at 3.0 V, i.e., at both the potentials, the layers contain  $\text{Nb}_2\text{O}_5$  and  $\text{Al}_2\text{O}_3$ , as evident from the positions of the Nb 3*d* and Al 2*p* spectra—207.8 and 74.8 eV.

In addition to titanium and oxygen, the surface layer formed on NiTi contains a small amount of nickel (Table 1). The high-resolution spectrum reveals that nickel is present as Ni metal and NiO, as evidenced by the peaks located at 852.9 and 856.4 eV (Fig. 4c). Therefore, the surface layer comprises nickel in both the metal and the oxidized states but the intensity of the oxide peak prevails. In our earlier investigation, the nickel metal peak was shown to disappear only after oxidation of Nitinol at potentials more positive than 0.7 V versus SCE [28].

### 3.1.3 In-depth composition and thickness of the oxide layer

The composition and the thickness of the layers formed by anodization are revealed by XPS analysis combined with ion sputtering. Depth profiles are presented in Figs. 5 and 6. The content of carbon decreased soon after the sputtering process began, in accordance with its presence as a surface contaminant. As the sputtering process proceeds and the surface oxide is sputtered away, the content of oxygen decreases progressively, while that of titanium increases (Fig. 5a). For Ti–6Al–7Nb alloy, the contents of Al and Nb also increase (Fig. 5b). Similar behavior of Ti and Ti–6Al–7Nb alloys was observed after oxidation at 3.0 V (Fig. 6). For NiTi alloy, the sputtering process induces a strong enrichment of nickel, due to preferential sputtering of this element (Fig. 5c) [29]. Two important issues are revealed, based on the depth profiles: the thickness of the layer and the in-depth chemical state of the particular elements.

The sputtering time at which oxygen content decreases to half of that at the surface is taken as a measure of thickness, the latter then being calculated taking into account the sputtering rate of 2 or 4 nm min<sup>−1</sup> relative to the  $\text{SiO}_2$  standard. From the shape of the decrease of oxygen concentration in the depth profile, it can be assumed that the thickest layer is formed on Ti metal.

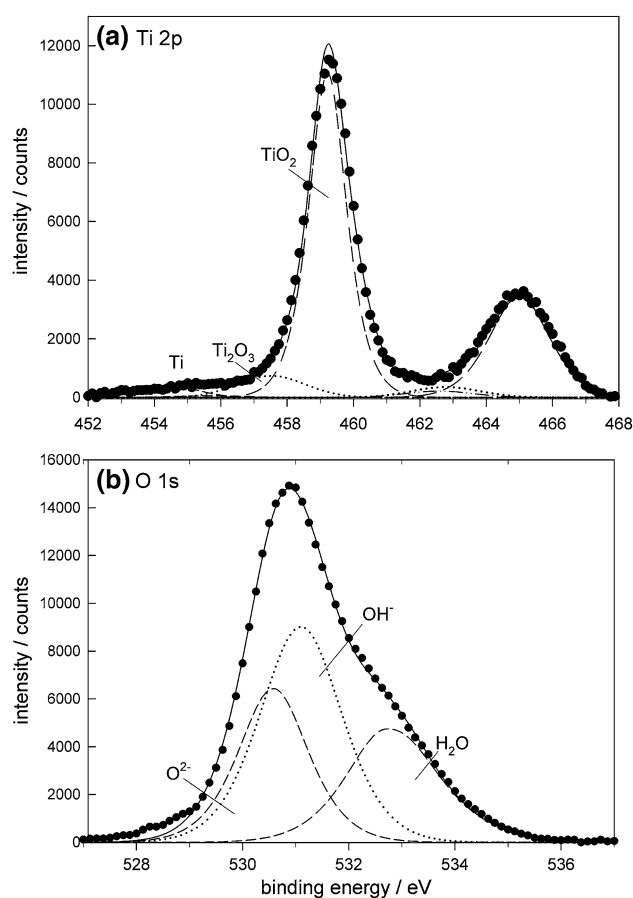


**Fig. 3** Deconvoluted XPS **a** Ti 2*p* and **b** O 1*s* spectra measured at the surface of Ti oxidized at 3.0 V for 2 h in 1 M acetic acid. Experimental spectrum (●●●), fitted spectrum (solid line), component peaks (dashed lines)

**Table 2** Intensity of particular component peaks in Ti 2*p* and O 1*s* deconvoluted XPS spectra measured at the surface of layers formed by potentiostatic oxidation at 0.7 and 3.0 V of Ti, Ti–6Al–7Nb, and NiTi in 1 M acetic acid (1 M, pH 2.3) for 2 h

Peak	Peak intensity(%)				
	$E_{\text{ox}} = 0.7 \text{ V}$			$E_{\text{ox}} = 3.0 \text{ V}$	
	Ti	Ti–6Al–7Nb	NiTi	Ti	Ti–6Al–7Nb
% Ti	4.6	3.1	4.5	4.8	3.3
% $\text{Ti}_2\text{O}_3$	9.6	10.0	12.5	9.4	11.1
% $\text{TiO}_2$	85.8	86.8	82.9	85.8	85.6
% $\text{O}^{2-}$	34.5	27.9	43.1	34.3	32.5
% $\text{OH}^-$	41.4	44.8	39.5	40.2	43.5
% $\text{H}_2\text{O}$	24.0	27.3	17.4	25.5	24.0

Oxidation potentials,  $E_{\text{ox}}$ , were 0.7 and 3.0 V

Indeed, the estimated thickness of the  $\text{TiO}_2$  layer during the anodization at 0.7 V is 30 nm on Ti, 12 nm on the Ti–6Al–7Nb alloy, and only 8 nm on Nitinol. During anodization at 3.0 V, the corresponding values are 60 nm on Ti, and

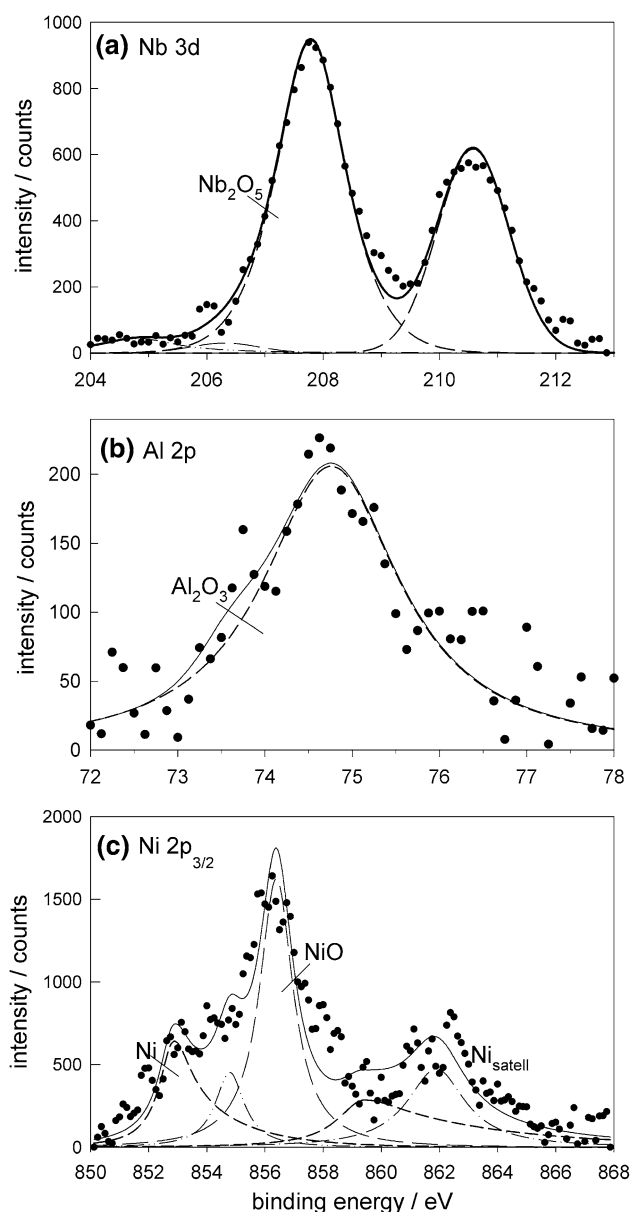


**Fig. 4** Deconvoluted XPS (a) Al 2p, and (b) Nb 3d spectra measured at the surface of Ti–6Al–7Nb oxidized at 3.0 V for 7,200 s in 1 M acetic acid. (c) deconvoluted Ni 2p spectrum measured at the surface of NiTi oxidized at 0.7 V for 2 h in 1 M acetic acid. Experimental spectrum (●●●), fitted spectrum (solid line), component peaks (dashed lines)

48 nm on the Ti–6Al–7Nb alloy. The thickness of the TiO<sub>2</sub> layer, therefore decreases in the order Ti > Ti–6Al–7Nb >> NiTi. These values of thickness agree with those reported in the literature. Sul et al. [13] reported values between 71 and 234.5 nm for galvanostatic oxidation of titanium in 1 M acetic acid at a constant current density of 5 mA cm<sup>−2</sup>. Lower values have been reported for Nitinol, galvanostatic oxidation of NiTi in 1 M acetic acid resulting in the formation of a TiO<sub>2</sub> layer 20–25-nm thick at 20 mA cm<sup>−2</sup> for 1 h [25], and a 100-nm thick layer in

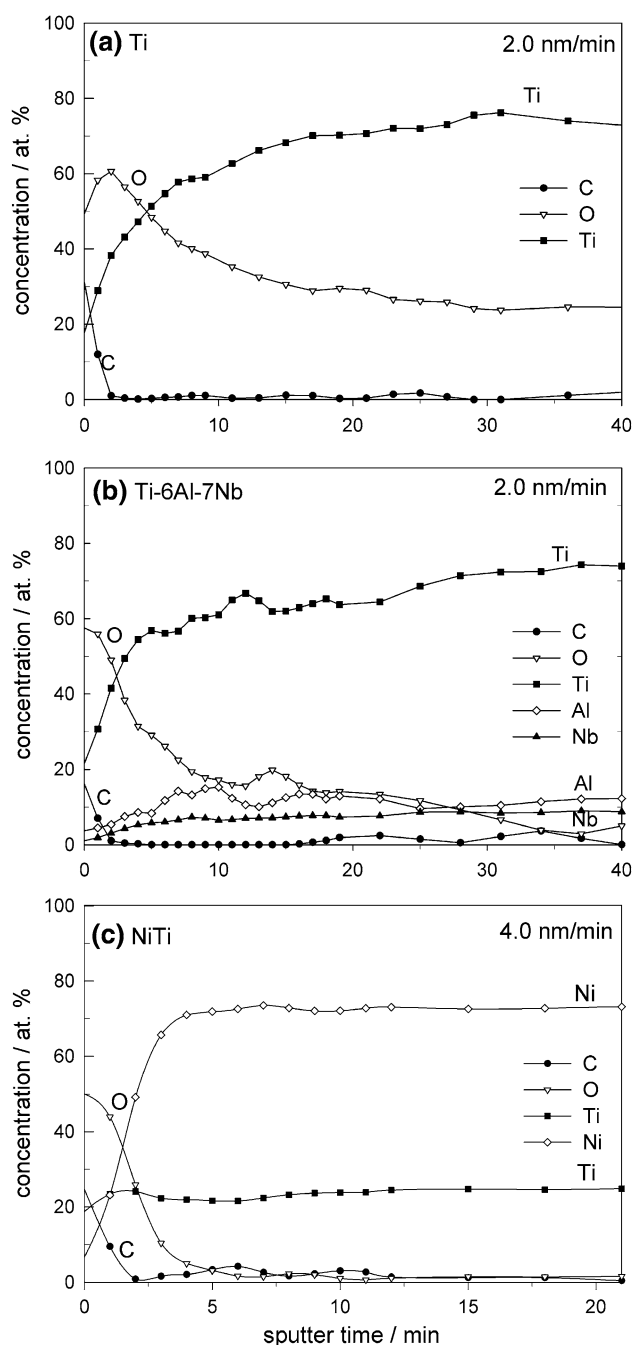


**Fig. 5** Depth profiles of layers formed on (a) Ti, (b) Ti–6Al–7Nb, and (c) NiTi oxidized at 0.7 V for 2 h in 1 M acetic acid. Sputter rate (a and b) 2.0 nm min<sup>−1</sup>, (c) 4.0 nm min<sup>−1</sup> relative to SiO<sub>2</sub> standard

0.02 M sodium sulphate solution at 0.3 mA for 1 h [27]. Thinner films, <10 nm, were produced by the potentiostatic oxidation of Nitinol in acetic acid [28].

The intensity of the oxygen peak decreases progressively with the increase in sputtering. It diminished after 8 min for NiTi, while, for Ti, it still persists after 21 min, indicating a difference in the layer thickness. A similar situation is observed for the Ti signal. The transition of the Ti 2p<sub>3/2</sub> peak from oxide (459.2 eV) to metal (454.5 eV)

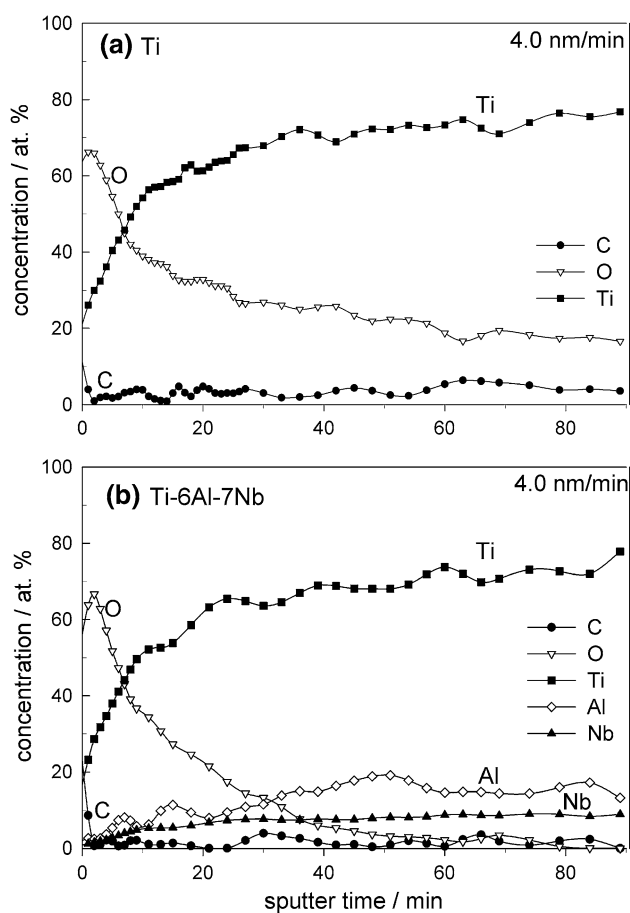


**Fig. 6** Depth profiles of layers formed on (a) Ti and (b) Ti-6Al-7Nb oxidized at 3 V for 2 h in 1 M acetic acid. Sputter rate 4.0 nm min<sup>-1</sup> relative to SiO<sub>2</sub> standard

**Table 3** The values of corrosion potential,  $E_{\text{corr}}$ , measured for Ti, Ti-6Al-7Nb and NiTi after stabilization period in aerated Hanks solution at pH 7.5 at 37 °C for untreated samples and samples oxidized at 0.7 and 3.0 V in acetic acid (1 M, pH 2.3) for 2 h

Sample	$E_{\text{corr}}$ (V)
Untreated	
NiTi	-0.551
Ti	-0.511
Ti-6Al-7Nb	-0.301
Oxidized at 0.7 V in acetic acid	
NiTi	-0.221
Ti	-0.020
Ti-6Al-7Nb	-0.084
Oxidized at 3.0 V in acetic acid	
Ti	-0.209
Ti-6Al-7Nb	-0.098

range is prolonged by up to 6 min relative to Ti, but it takes only 2 min for NiTi (data not shown). It is of interest to consider the behavior of minor oxides. For the anodized

layer on NiTi, nickel is present as NiO (856.5 eV) only at the surface; as soon as the sputtering begins the peak center shifts to the range of nickel metal (851.8 eV). This means that, in the anodized layer, it is present as metal and not as oxide. On the other hand, the minor oxides formed in the TiO<sub>2</sub> layer on the Ti-6Al-7Nb alloy are present as oxides Al<sub>2</sub>O<sub>3</sub> and Nb<sub>2</sub>O<sub>5</sub> within the TiO<sub>2</sub> layer i.e., in the upper part of the layer where these oxides are preferentially located [36].

### 3.2 The effect of anodization on corrosion measurements in SPS

#### 3.2.1 Open circuit potential and linear polarization measurements

The chemical properties of the oxide layer play an important role in the biocompatibility of titanium implants and their surrounding tissues. Oxide layers must not break down if the implant is to be successful [38–40]. Chemical interaction of a metallic material of the prosthesis with the body fluid in the environment is important for the stability of an implant in the human body. This behavior was simulated by the corrosion tests in simulated Hanks physiological solution. A shift of the open circuit potential in the positive direction indicates the formation of a passive film, while a decrease indicates breaks in the film, dissolution of the film, or absence of film formation [41]. For all the three materials, the values of  $E_{\text{oc}}$  increased with the immersion time, indicating the formation of a protective oxide film in SPS. The values of  $E_{\text{corr}}$  after stabilization for 2 h were -0.551 V for Ti, -0.511 V for Ti-6Al-7Nb alloy, and -0.301 V for NiTi (Table 3). The value for Nitinol is approximately 250 mV more positive than those for the two other materials. This is probably the effect of the nickel content in the alloy. In terms of corrosion, nickel is less resistant than titanium and Ti-6Al-7Nb alloy [24].

After anodization in acetic acid, the curves are strongly shifted to more positive potentials, indicating that the presence of a thick oxide layer protects the underlying material (Table 3). The values of  $E_{\text{corr}}$  reached at the end of the stabilization period were up to 530 mV more positive than those obtained with the untreated samples: -0.020 V for Ti, -0.084 V for Ti-6Al-7Nb alloy, and -0.221 V for NiTi after oxidation at 0.7 V in acetic acid, and -0.209 V for Ti and -0.098 V for Ti-6Al-7Nb alloy after oxidation at 3.0 V in acetic acid.

The values of polarization resistance,  $R_p$ , were calculated from the slope of  $j$  versus  $E$  curves measured over a narrow range around  $E_{\text{corr}}$  (Table 4). These values that reflect the resistance to general corrosion, differ significantly between the three materials, decreasing in the order Ti-6Al-7Nb > Ti > NiTi. The value for Ti-6Al-7Nb is



**Table 4** Corrosion parameters measured in simulated physiological solution, pH 7.4,  $T = 37\text{ }^{\circ}\text{C}$ , for untreated Ti, Ti–6Al–7Nb, and NiTi, and after oxidation in 1 M acetic acid for 2 h

Sample/corrosion parameters	$R_p$ ( $\text{k}\Omega\text{ cm}^2$ )	Ratio ( $R_p$ )	$E_{\text{corr}}$ (V)	$j_{\text{corr}}$ ( $\text{nA cm}^{-2}$ )	Ratio ( $j_{\text{corr}}$ )	$E'_{\text{corr}}$ (V)	$\Delta E$ (V)	$\Delta E'$ (V)
Untreated								
Ti	476		−0.579	97.90		0.693	6.579	5.307
Ti–6Al–7Nb	992		−0.526	48.36		0.467	6.526	5.533
NiTi	253		−0.278	423.0		−0.103	0.778	0.603
Oxidized at 0.7 V in acetic acid								
Ti	1,719	+3.6	−0.080	9.59	−10.2	0.273	6.080	5.727
Ti–6Al–7Nb	1,853	+1.9	−0.139	6.35	−7.6	0.637	6.139	5.363
NiTi	695	+2.7	−0.304	2.474	−170.1	−0.100	0.804	0.600
Oxidized at 3.0 V in acetic acid								
Ti	669	+1.4	−0.274	6.623	−14.8	0.498	6.274	5.502
Ti–6Al–7Nb	1,197	+1.2	−0.234	1.268	−38.1	0.717	6.234	5.283

Polarization resistance,  $R_p$ , was determined from linear polarization measurements. Characteristic parameters deduced from cyclic polarization curves are: corrosion potential in the forward and reverse scan,  $E_{\text{corr}}$  and  $E'_{\text{corr}}$ , corrosion current density,  $j_{\text{corr}}$ , span of the corrosion stability in the forward and reverse scan,  $\Delta E = (E_{\text{sw}} - E_{\text{corr}})$  and  $\Delta E' = (E_{\text{sw}} - E'_{\text{corr}})$ . Switching potential,  $E_{\text{sw}}$ , was 6 V for Ti and Ti–6Al–7Nb, and 0.5 V for NiTi. Ratio  $R_p$ , and ratio  $j_{\text{corr}}$  are the ratios between  $R_p$  and  $j_{\text{corr}}$  for untreated and oxidized samples, respectively

four times larger than that for NiTi, while the value for Ti is in between these two values. Due to the formation of the oxide layer by anodization in acetic acid, the protective ability of the surface is strongly increased, as evidenced by an increase in the  $R_p$  values (Table 4). The highest value of polarization resistance is that of the Ti–6Al–7Nb alloy anodized at 0.7 V, i.e., about  $1.8\text{ M}\Omega\text{ cm}^2$ . Comparison of the values before and after oxidation shows that the highest relative increases are those for titanium oxidized at 0.7 V (3.6 times) and Nitinol (2.7 times).

### 3.2.2 Cyclic polarization measurements

CP curves for Ti metal, Ti–6Al–7Nb, and NiTi alloys, both untreated and following anodization in acetic acid, were measured in SPS (Figs. 7, 8, 9). The switching potential,  $E_{\text{sw}}$ , was 6 V for Ti and Ti–6Al–7Nb alloy, and 0.5 V for NiTi alloy. While the former two show a broad passive range extending up to 8 V, NiTi exhibits a much narrower range of stability and is susceptible to localized corrosion breakdown at potentials more positive than 0.52 V [24]. The method of CP is usually used to determine the parameters characteristic of localized corrosion, e.g., breakdown and repassivation potentials [31]. Since Ti and Ti–6Al–7Nb alloy are not susceptible to localized corrosion in SPS [42], and Nitinol is susceptible to localized corrosion at potentials more positive than  $E_{\text{sw}}$  of 0.5 V, these parameters are not relevant for the present measurements. Instead, the following corrosion parameters were deduced from the curves measured: corrosion potential,  $E_{\text{corr}}$ , and the corrosion current density,  $j_{\text{corr}}$ , deduced using Tafel extrapolation and the Stern–Geary interpretation. Two parameters were defined as the measures of the corrosion stability (Table 4)—the difference between

the switching potential,  $E_{\text{sw}}$ , and the corrosion potential measured in forward and reverse scans:  $\Delta E = E_{\text{sw}} - E_{\text{corr}}$  and  $\Delta E' = E_{\text{sw}} - E'_{\text{corr}}$ . The larger the values of  $\Delta E$  and  $\Delta E'$ , more stable the oxide layer in the forward and reverse scans.

Consider first, the curves for materials without anodization. The values of  $R_p$  and  $j_{\text{corr}}$  are inversely proportional to each other; high  $R_p$  values are related to low values of  $j_{\text{corr}}$ . Values of  $j_{\text{corr}}$  increase as follows: Ti–6Al–7Nb < Ti << NiTi, i.e., the reverse of those for  $R_p$  (Table 4). Following the Tafel region the current densities for Ti and Ti–6Al–7Nb increase rapidly up to the first anodic plateau which extends from −0.2 to 1.0 V (Figs. 7, 8). The second current density plateau is then formed, extending up to the  $E_{\text{sw}}$ . For Ti metal, a slight increase of current density with increasing potential is observed in the second current plateau, while for the Ti–6Al–7Nb alloy the current density is constant. The values of  $\Delta E$  are similar for Ti metal (6.579 V) and Ti–6Al–7Nb alloy (6.526 V), and much smaller for NiTi alloy (0.778 V), proving its lower stability to corrosion (Fig. 9). After scan reversal, the current density decreases, confirming that there was no localized corrosion event, since otherwise an increase in current density would occur [31]. For Ti and Ti–6Al–7Nb alloy, the values of  $\Delta E'$  are approximately 1 V smaller than the  $\Delta E$  values in the forward scan (Table 4). For NiTi, on the other hand, these two values are similar. In other words, the difference ( $E'_{\text{corr}} - E_{\text{corr}}$ ) is largest for Ti (1.28 V) and smallest for NiTi (0.08 V).

The formation of an oxide layer by anodization in acetic acid strongly affects the polarization behavior of the materials investigated (Figs. 7, 8, 9). The shapes of the curves are changed and, consequently, also the values of the characteristic corrosion parameters (Table 4). After

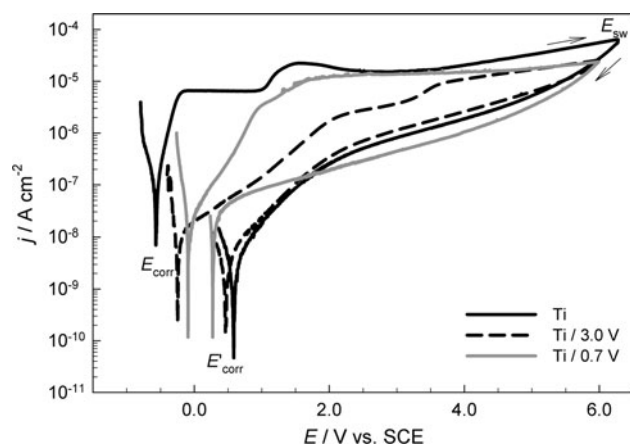


**Fig. 7** Cyclic polarization curves measured in simulated physiological solution, pH 7.4,  $T = 37^\circ\text{C}$ , for untreated Ti and, after oxidation of Ti at 0.7 and 3.0 V, in 1 M acetic acid for 2 h. Scan rate  $1\text{ mV s}^{-1}$ . Characteristic parameters  $E_{\text{corr}}$ ,  $E'_{\text{corr}}$ , and  $j_{\text{corr}}$  are listed in Table 4. The switching potential,  $E_{\text{sw}}$ , was 6.0 V

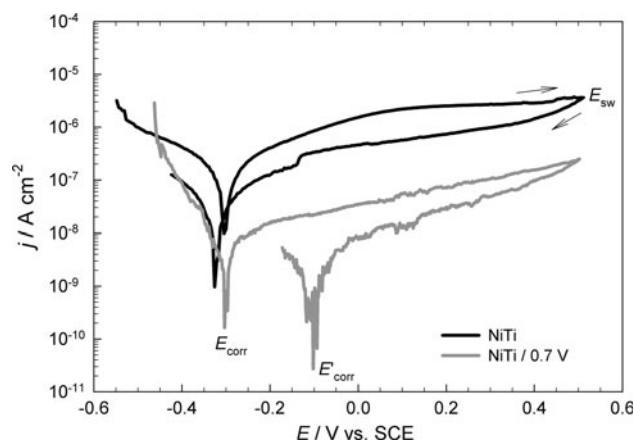


**Fig. 9** Cyclic polarization curves measured in simulated physiological solution, pH 7.4,  $T = 37^\circ\text{C}$ , for untreated NiTi, and after oxidation of NiTi at 0.7 V in 1 M acetic acid for 2 h. Scan rate  $1\text{ mV s}^{-1}$ . Characteristic parameters  $E_{\text{corr}}$ ,  $E'_{\text{corr}}$ , and  $j_{\text{corr}}$  are listed in Table 4. Switching potential,  $E_{\text{sw}}$ , was 0.5 V

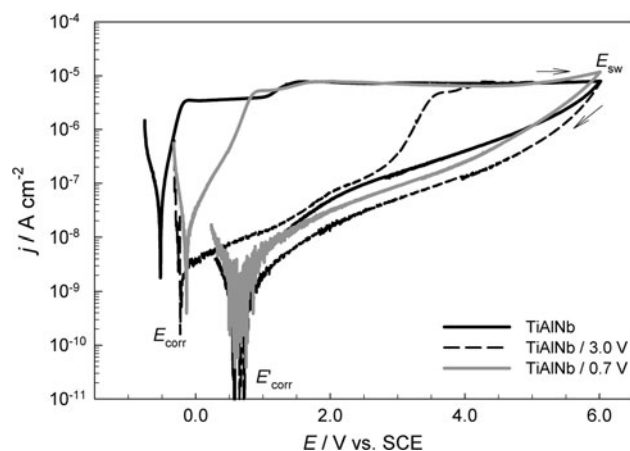


**Fig. 8** Cyclic polarization curves measured in simulated physiological solution, pH 7.4,  $T = 37^\circ\text{C}$ , for untreated Ti-6Al-7Nb, and after oxidation of Ti-6Al-7Nb at 0.7 and 3.0 V in 1 M acetic acid for 2 h. Scan rate  $1\text{ mV s}^{-1}$ . Characteristic parameters  $E_{\text{corr}}$ ,  $E'_{\text{corr}}$ , and  $j_{\text{corr}}$  are listed in Table 4. Switching potential,  $E_{\text{sw}}$ , was 6.0 V

anodization the  $E_{\text{corr}}$  values are shifted by approximately 300–500 mV in a more positive direction for Ti and Ti-6Al-7Nb alloy, while for NiTi, the shift is only 20 mV. More pronounced differences, of up to two orders of magnitude, are observed for the values of  $j_{\text{corr}}$ . The lowest absolute value of  $j_{\text{corr}}$  was obtained for the Ti-6Al-7Nb alloy; however, the relative decrease of  $j_{\text{corr}}$  was largest for NiTi (170 times) (Table 4). These results prove the strong increase of the corrosion resistance in SPS induced by the presence of an anodized oxide layer.

The potential of anodization in acetic acid affects the shape of the curve recorded subsequently in SPS. After anodization at 0.7 V, the first current plateau is absent and the values of current density are up to two orders of magnitude lower than those for the untreated sample

(Figs. 7, 8). Close to the beginning of the second current density plateau, the two curves cross and the current density of the untreated sample is reached. After oxidation at 3.0 V, the current density is further decreased, by up to three orders of magnitude. It reaches the curve of the untreated sample approximately in the middle of the well-developed passive region at  $\sim 4\text{ V}$ . After the scan reversal, the curves for untreated and oxidized samples remain similar. The values of  $\Delta E$  and  $\Delta E'$  are again close for Ti metal and Ti-6Al-7Nb alloy; the values are slightly lower than for untreated samples due to the shift of  $E_{\text{corr}}$  to more positive values. The decrease in the current density of the polarization curve for Nitinol is about two orders of magnitude in both forward and reverse scans (Fig. 9).

### 3.2.3 Electrochemical impedance spectroscopy

The potentiodynamic polarization measurements (Figs. 7, 8, 9) revealed that, of the three titanium-based materials, Ti-6Al-7Nb alloy possesses the greatest corrosion resistance in simulated Hanks physiological solution at pH 7.4 and  $37^\circ\text{C}$ , this behavior being valid for the untreated samples as well as for the samples oxidized at 3.0 V in acetic acid. Therefore, EIS was focused on this material to study the influence of immersion time on the corrosion behavior of untreated and oxidized Ti-6Al-7Nb alloy samples in SPS.

Spectra were recorded at various times of immersion of the untreated and oxidized Ti-6Al-7Nb sample at the open circuit potential in SPS. The results are displayed as Bode and phase angle diagrams (Fig. 10). The system exhibits a highly capacitive behavior over a relatively wide-frequency region, as indicated by phase angles approaching

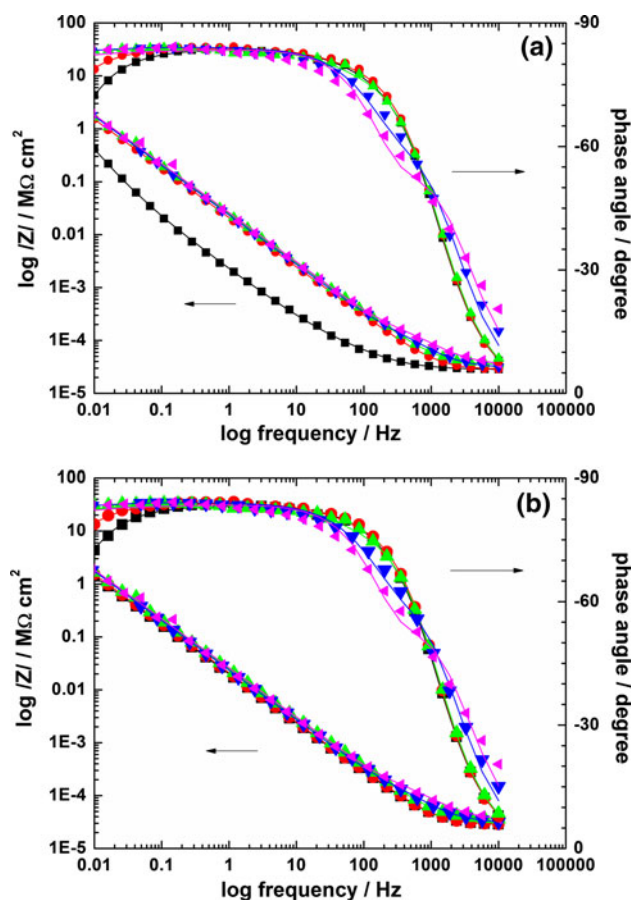


**Fig. 10** Bode diagrams recorded at different immersion times for **a** untreated Ti-6Al-7Nb alloy and **b** oxidized Ti-6Al-7Nb alloy (at 3.0 V in acetic acid) at  $E_{oc}$  in simulated physiological solution, at 37 °C. Immersion times (h): (filled square) 0; (filled circle) 1; (filled triangle) 15; (filled inverted triangle) 48; (filled right-pointing triangle) 140; (○) simulated data

90°, suggesting that a stable passive film is formed on Ti-6Al-7Nb alloy in SPS. The impedance response evolves with the time of immersion in the corrosive solution. The large peak in the phase angle observed on the impedance diagrams for both untreated and oxidized Ti-6Al-7Nb samples at different immersion times could indicate the interaction of at least two time constants [43]. Consequently, the whole set of impedance data was interpreted using the equivalent circuit given (Fig. 11), which describes the electrochemical behavior of a metal covered with an unsealed porous film and was previously used to simulate the oxide films formed on Ti-based materials immersed in a phosphate buffer-saline solution [44, 45] and on Ti-6Al-7Nb [36] and Ti-13Nb-13Zr [46] alloys in Hanks physiological solution at 37 °C. The equivalent circuit is based on a two-layer structure of the passive film—a dense inner layer and a porous outer layer. The latter contains microscopic pores, whereas the barrier layer is compact and exhibits a very large resistance [46]. In this

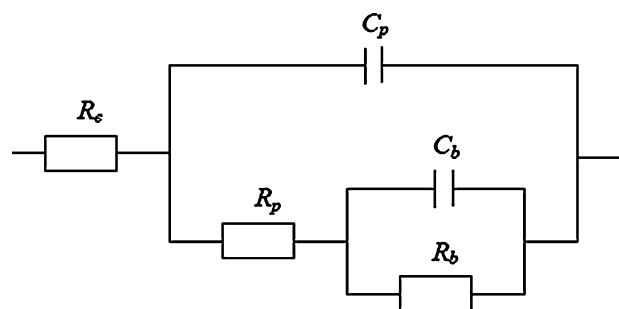


**Fig. 11** Equivalent circuit used for interpreting the experimental impedance data

two-layer oxide approach,  $R_s$  is the solution resistance, the parameters  $R_p$  and  $C_p$  describe the reactions at the outer porous passive film/solution interface, and the parameters  $R_b$  and  $C_b$  parameters are attributed to the processes at the inner barrier layer at the electrolyte/passive film interface.

In order to obtain a more accurate fit to the experimental data, the elements represented in both circuits as capacitors  $C_b$  and  $C_p$  were fitted as constant phase elements (CPEs) represented by the terms,  $Q$  and  $n$  [36]. The impedance of the CPE is given by [47]:

$$Q = Z_{CPE(\omega)} = [C(j\omega)^n]^{-1} \quad (1)$$

where  $j$  is an imaginary number and  $\omega$  is the angular frequency in  $\text{rad s}^{-1}$ ; depending on the value of the exponent  $n$ , CPE could be a resistor with resistance  $R$  ( $n = 0$ ); a capacitor with capacitance  $C$  ( $n = 1$ ); a Warburg impedance,  $W$  ( $n = 0.5$ ) or an inductance,  $L$  ( $n = -1$ ). The values of  $n$  are associated with the nonuniform distribution of current as a result of roughness and surface defects.

The values of the equivalent circuit component obtained by adjusting the experimental data, using the equivalent circuit illustrated in Fig. 11, are shown in Table 5. The quality of the fitting procedure was evaluated by the Chi squared ( $\chi^2$ ) values, which were of the order of  $10^{-4}$ – $10^{-3}$ . Another factor confirming that the equivalent circuit used reproduces the impedance data correctly is revealed in Fig. 10, where very good agreement between the experimental and simulated data was obtained at different immersion times. In order to compare the capacitance values for Ti-6Al-7Nb alloy at different immersion times, the values of CPEs from Table 5 were recalculated using the equation [35]:

$$C = [R^{1-n}Q]^{1/n} \quad (2)$$

As seen in Table 5, in the case of the untreated Ti-6Al-7Nb sample, the values of  $R_p$  are low, suggesting the formation of a porous layer with a very low resistance on the alloy surface [36]. The resistance of the porous layer increases in the first hours of immersion from  $0.53 \text{ k}\Omega \text{ cm}^2$  at the beginning of the experiment to  $1.24 \text{ k}\Omega \text{ cm}^2$  after 15 h immersion. Further increase in the immersion time leads to a

decrease of the  $R_p$  values. In addition,  $C_p$  is relatively low and decreases during the immersion period from  $14.23 \mu\text{F cm}^{-1}$  at the beginning of experiment to  $4.15 \mu\text{F cm}^{-2}$  after 140 h (Table 5). A similar variation of the porous layer parameters,  $R_p$  and  $C_p$ , with immersion time was also observed for the oxidized Ti–6Al–7Nb alloy (Table 5). However, especially at low immersion times, the porous layer resistance corresponding to the oxidized alloy is at least one order of magnitude higher than those corresponding to the untreated samples, while the values of  $C_p$  are smaller.

In order to explain these variations of the  $R_p$  and  $C_p$  parameters with immersion time, it was assumed that the porous layer formed on both untreated and oxidized alloy surfaces in the first 15 h of immersion to SPS can become thicker due to slow growth of the oxide layer, but that, at

longer immersion times, some cracks or defects (pores) could appear, leading to a re-enhancement of the corrosion process. Nevertheless, at the longest immersion times, the  $C_p$  and  $R_p$  values reach approximately constant values, suggesting long-term stability of the passive film.

For both untreated and oxidized samples, the  $R_b$  values are up to three orders of magnitude greater than those associated with the outer porous layer (Table 5), suggesting the formation of a barrier layer with high corrosion protection ability. At all immersion times, the resistances of the barrier layer corresponding to the oxidized alloy are significantly higher than those determined for the untreated sample, confirming the beneficial effect of the anodic oxidation procedure on the corrosion behavior of the Ti–6Al–7Nb alloy.

**Table 5** Values of fitted parameters of the equivalent circuit as a function of the immersion time of untreated and oxidized Ti–6Al–7Nb alloy in simulated physiological solution

Time (h)	$R_e$ ( $\Omega \text{ cm}^2$ )	$R_p$ ( $\text{k}\Omega \text{ cm}^2$ )	$Q_p$ ( $\mu\Omega^{-1} \text{ s}^n \text{ m}^{-2}$ )	$n_1$	$C_p$ ( $\mu\text{F cm}^{-2}$ )	$R_b$ ( $\text{M}\Omega \text{ cm}^2$ )	$Q_b$ ( $\mu\Omega^{-1} \text{ s}^n \text{ cm}^{-2}$ )	$n_2$	$C_b$ ( $\mu\text{F cm}^{-2}$ )
Untreated									
0	26.96	0.53	14.3	0.998	14.23	0.57	13.36	0.848	19.25
1	31	0.64	12.9	0.997	12.76	0.90	14.45	0.837	23.79
2	30.13	0.78	14.5	0.976	13.03	0.91	10.55	0.896	13.70
4	29.89	0.95	16.4	0.939	12.59	1.47	8.759	0.832	14.66
6	26.77	1.07	17.9	0.899	11.57	2.95	7.35	0.906	10.09
8	34.22	1.17	14.4	0.908	9.53	4.52	6.69	0.918	9.05
10	37.24	1.20	13.6	0.916	9.33	5.55	5.58	0.901	8.14
15	40.06	1.24	10.3	0.914	6.82	4.58	6.72	0.914	9.27
24	31.87	0.35	9.62	0.913	5.59	5.33	1.11	0.879	1.43
48	34.17	0.40	9.81	0.856	3.86	6.84	11.70	0.890	20.07
72	40.3	0.57	10.1	0.855	4.23	8.85	9.33	0.890	16.08
96	36.17	0.41	10.9	0.872	4.95	9.88	12.81	0.872	26.00
120	38.28	0.41	10.4	0.869	4.57	19.53	10.24	0.888	19.99
140	43.37	0.54	8.11	0.890	4.15	22.91	8.82	0.902	15.71
Oxidized at 3.0 V in acetic acid									
0	28.26	5.22	8.67	0.928	6.84	7.06	0.47	0.937	0.51
1	28.63	9.56	8.22	0.932	6.83	17.90	0.40	0.943	0.45
2	26.54	17.69	8.06	0.933	7.01	20.95	0.44	0.967	0.47
4	28.64	9.03	8.08	0.932	6.67	24.01	0.50	0.944	0.58
6	28.4	11.27	7.55	0.929	6.27	25.35	0.61	0.937	0.74
8	28.15	7.16	7.69	0.927	6.13	30.95	0.59	0.949	0.68
10	34.95	2.57	7.40	0.927	5.41	55.38	0.80	0.933	1.05
15	29.78	1.33	6.80	0.927	4.70	65.63	0.88	0.928	1.21
24	30.75	1.03	6.48	0.928	4.39	91.60	0.93	0.915	1.41
48	32.59	0.79	5.16	0.931	3.44	101.9	1.47	0.922	2.24
72	40.3	0.65	5.12	0.913	2.97	130.3	1.76	0.952	2.31
96	36.86	0.41	4.66	0.947	3.28	110.4	2.04	0.920	3.26
120	34.06	0.42	4.87	0.943	3.35	131	2.46	0.958	3.17
140	28.26	0.34	4.86	0.919	2.78	110.8	2.18	0.938	3.13



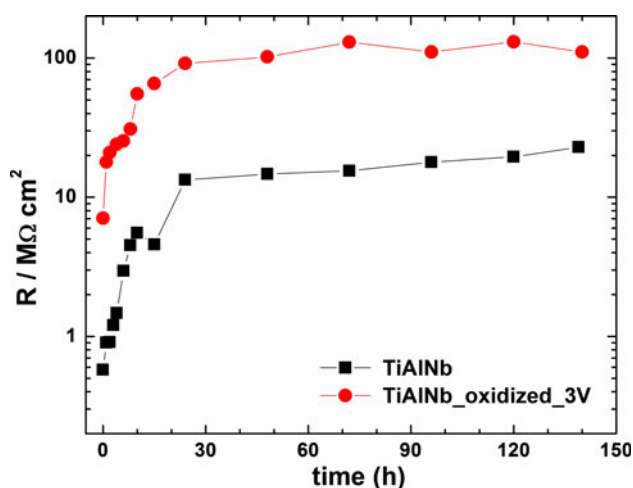


**Fig. 12** Evolution of polarization resistance presented as the sum of partial resistances as a function of the immersion time in SPS

Moreover, a significant increase of the  $R_b$  values with immersion time was observed for both untreated and oxidized samples. The values of resistance of the barrier layer formed in the first hours of immersion in SPS are in agreement with those reported [36, 48] and they increase progressively in time, from  $0.57 \text{ M}\Omega \text{ cm}^2$  at the beginning of the experiment to  $22.91 \text{ M}\Omega \text{ cm}^2$  after 140 h of immersion in SPS. For the oxidized sample,  $R_b$  has an initial value of  $7.06 \text{ M}\Omega \text{ cm}^2$  at  $t = 0 \text{ h}$  which increases up to 15 times during the immersion period, reaching  $110.8 \text{ M}\Omega \text{ cm}^2$  at the end of the experiment.

The barrier layer capacitance of the untreated sample decreases in the first 24 h of immersion in SPS, then increases at higher immersion times while, in the case of oxidized alloy, the  $C_b$  values gradually increase with time. The values of  $n_1$  and  $n_2$  for the oxidized Ti–6Al–7Nb samples are in the range 0.913–0.967; hence, CPE1 and CPE2 corresponding to the oxidized alloy could be considered approximately as pure capacitors. The  $n_2$  values corresponding to untreated Ti–6Al–7Nb alloy lay in the range 0.832–0.914, while a decrease of the  $n_1$  values was observed at high-immersion times, probably as a consequence of the increase in heterogeneity and roughness of the porous oxide layer.

The variation of the overall polarization resistance,  $R$ , calculated as the sum of the resistance values, determined by a fitting procedure from impedance data for untreated and oxidized samples, is presented in Fig. 12. The values of the polarization resistance increase markedly in time, and this behavior is more pronounced for the oxidized alloy. Therefore, it can be concluded that the oxide layer formed by anodic oxidation on the Ti–6Al–7Nb surface is an effective anticorrosive layer, which, to a great extent, hinders the corrosion processes occurring at the metal substrate interface.

## 4 Conclusions

Formation of the oxide layer on Ti-based materials—Ti metal and Ti–6Al–7Nb and NiTi alloys—in acetic acid was studied at two potentials of interest 0.7 and 3.0 V. Regardless of the substrate, the main oxide component formed was titanium(IV) oxide,  $\text{TiO}_2$ . The layer formed on Ti–6Al–7Nb alloy contained oxides of minor elements,  $\text{Al}_2\text{O}_3$  and  $\text{Nb}_2\text{O}_5$ , while the layer formed on Nitinol contained a small amount of nickel. While the composition of the oxide layer is similar on all the three substrates, its thickness differs according to the oxidation potential and type of substrate. The thickness increases in the following order as a function of substrate: NiTi < Ti–6Al–7Nb < Ti. The thickness increases with the increasing oxidation potential.

Anodization in acetic acid, and the resulting formation of  $\text{TiO}_2$  at the substrate, affects beneficially the corrosion behavior of all the three materials in SPS. Of the three materials, the Ti–6Al–7Nb alloy expresses the most protective corrosion behavior in SPS, while Nitinol alloy yields the poorest corrosion performance.

The polarization resistance values, determined from EIS measurements for the oxidized Ti–6Al–7Nb alloy during the later stages of immersion, are one order of magnitude higher than those determined for the untreated alloy. Thus, the anodized samples possess a much higher corrosion resistance than the untreated ones. The significant enhancement of the polarization resistance values at the longer immersion time in SPS could be due to the stabilization of the barrier layer, which might diminish the tendency of the alloy to corrosion. This study shows that anodization provides a simple and effective means of improving the corrosion behavior of different titanium-based alloys in SPS.

**Acknowledgments** The authors gratefully thank the financial support within the project *Investing in people!*, a Ph.D. scholarship, and co-financing by the Sectorial Operational Program For Human Resources Development 2007–2013, **Priority Axis 1**. “Education and training in support for growth and development of a knowledge based society”, **Key area of intervention 1.5**: Doctoral and post-doctoral programs in support of research, Contract nr: **POSDRU/88/1.5/S/60185**—“Innovative Doctoral Studies In A Knowledge Based Society” the Babeş-Bolyai University, Cluj-Napoca, Romania. The authors thank the valuable technical help of B. Kapun, G. Žerjav, M. Seručnik and P. Rodič of the Jožef Stefan Institute during the stay of Diana Blejan. The financial support of this study provided by the Slovenian Research Agency within the research grant P2-0148 is greatly appreciated.

## References

1. Popa MV, Calderon Moreno JM, Popa M, Vasilescu E, Drob P, Vasilescu C, Drob SI (2011) Surf Coat Technol 205:4776
2. Cui X, Kim H-M, Kawashita M, Wang L, Xiong T, Kokubo T, Nakamura T (2009) Dent Mater 25:80



3. Santillan MJ, Quaranta NE, Boccaccini AR (2010) *Surf Coat Technol* 205:2562
4. Fu G, Vary PS, Lin C-T (2005) *J Phys Chem B* 109:8889
5. Moskalewicz T, Czyrska-Filemonowicz A, Boccaccini AR (2007) *Surf Coat Technol* 201:7467
6. Mai L, Wang D, Zhang S, Xie Y, Huang C, Zhang Z (2010) *Appl Surf Sci* 257:974
7. Amin SA, Pazouki M, Hosseinnia A (2009) *Powder Technol* 196:241
8. Boskovic I, Mentus SV, Pjescic M (2006) *Electrochim Acta* 51:2793
9. Yu B, Leung KM, Guo Q, Lau WM, Yang J (2011) *Nanotechnology* 22:115603
10. Boccaccini AR, Keim S, Ma R, Li Y, Zhitomirsky I (2010) *J R Soc Interface* 7:S581
11. Hassan AK, Chaure NB, Ray AK, Nabok AV, Habesch S (2003) *J Phys D* 36:1120
12. Aladjem A (1973) *J Mater Sci* 8:688
13. Sul Y-T, Johansson CB, Jeong Y, Alkerstsson T (2001) *Med Eng Phys* 23:329
14. Afshar A, Vaezi MR (2004) *Surf Coat Technol* 186:398
15. Liu X, Chu PK, Ding C (2004) *Mater Sci Eng R* 47:49
16. Prusi A, Arsov Lj, Haran B, Popov BN (2002) *J Electrochem Soc* 149:B491
17. Arsov LjD, Kormann C, Plieth W (1991) *J Electrochem Soc* 138:2964
18. Zwilling V, Darque-Ceretti E, Boutry-Forveille A, David D, Perrin MY, Aucouturier M (1999) *Surf Inter Anal* 27:639
19. Bracken WM, Sharma RP, Elsner YY (1985) *Cell Biol Toxicol* 4:259
20. Sabbioni E, Pozzi G, Pintar A, Casella L, Garattini S (1991) *Carcinogenesis* 12:47
21. Disegi JA (2000) *Inj Int J Care Inj* 31:S-D-14
22. Shabalovskaya S, Anderegg J, Van Humbeeck J (2008) *Acta Biomater* 4:447
23. Poncet PP (2000) Nitinol medical device design considerations. In: *Proceedings of International conference on shape memory and superelastic technology*, Asilomar, CA, p 441 [www.memry.com/resources/files/NiTi\\_devicedesign.pdf](http://www.memry.com/resources/files/NiTi_devicedesign.pdf)
24. Milošev I, Kapun B (2012) *Mat Sci Eng C* 32:1087
25. Shi P, Cheng FT, Man HC (2007) *Mater Lett* 61:2385
26. Cheng FT, Shi P, Pang GPH, Wong MH, Man HC (2007) *J Alloy Compd* 438:238
27. Chu CL, Wang RM, Hu T, Yin LH, Pu YP, Lin PH, Dong YS, Guo C, Chung CY, Yeung KWK, Chu PK (2009) *J Mater Sci Mater Med* 20:223
28. Metikoš-Huković M, Katić J, Milošev I (2012) *J Solid State Electrochem* 16:2503
29. Milošev I, Kapun B (2012) *Mat Sci Eng C* 32:1068
30. Milošev I, Metikoš-Huković M, Petrović Ž (2012) *Mat Sci Eng C* 32:2604
31. Szklarska-Smialowska Z (1986) *Pitting Corrosion of Materials*. National Association of Corrosion Engineers, Houston
32. <http://www.rbdinstruments.com>
33. Wolff M (1992) Thesis. Heinrich-Heine Universität, Düsseldorf
34. Seah MP, Dench W-A (1979) *Surf Inter Anal* 1:2
35. Milošev I, Metikoš-Huković M, Strehblow H-H (2000) *Biomaterials* 21:2103
36. Milošev I, Kosec T, Strehblow H-H (2008) *Electrochim Acta* 53:3547
37. Milošev I, Strehblow H-H (2000) *J Biomed Mater Res* 52:404
38. Al-Mobarak NA, Al-Swayih AA, Al-Rashoud FA (2011) *Inter J Electrochem Sci* 6:2031
39. Arslan H, Celikkan H, Örnek N, Ozan O, Ersoy AE, Aksu ML (2008) *J Appl Electrochem* 38:853
40. Songür M, Celikkan H, Gökmeşe F, Şimşek SA, Altun NŞ, Aksu ML (2009) *J Appl Electrochem* 39:1259
41. Gurappa I (2002) *Mater Character* 49:73
42. Milošev I (2011) *Pure Appl Chem* 83:309
43. Luiz de Assis S, Wolynek S, Costa I (2006) *Electrochim Acta* 51:1815
44. Aziz-Kerrzo M, Conroy KG, Fenelon AM, Farrell ST, Breslin CB (2001) *Biomaterials* 22:1531
45. Pan J, Thierry D, Leygraf C (1996) *Electrochim Acta* 41:1143
46. de Luiz Assis S, Costa I (2007) *Mater Res* 10:293
47. Raistrick D, MacDonald JR, Francschetti DR (1987) In: MacDonald JR (ed) *Impedance Spectroscopy Emphasizing Solid Materials and Systems*. J. Wiley & Sons, New York
48. Lavos-Valereto I, Wolynek S, Ramires I, Guastaldi AC, Costa I (2004) *J Mater Sci Mater Med* 15:55